



Aerodynamic Forces Acting on Ahmed-Type Vehicles under Fluctuating Headwind Conditions

M. Sumida^{1†} and K. Hayakawa²

¹ Faculty of Engineering, Kindai University, Higashi-Hiroshima, 739-2116, Japan

² Graduate School of Systems Engineering, Kindai University, Higashi-Hiroshima, 739-2116, Japan

†Corresponding Author Email: sumida7_2@air.ocn.ne.jp

(Received October 22, 2018; accepted January 19, 2019)

ABSTRACT

Aerodynamic forces of Ahmed-type road vehicles subjected to atmospheric fluctuation were studied in an advanced wind tunnel with programmable settings enabling the generation of pulsating wind speeds. The experiments were performed with a time-averaged airflow speed of approximately 13 m/s, with the fluctuating speed ranging from 2.58 to 2.90 m/s, and periods ranging from 1.5 to 5.0 s. The results of the time-dependent drag and lift forces acting on the vehicle were compared with those under steady wind conditions. Further, the influence of the rear slant angle of the Ahmed model on the forces was addressed. The fluctuation in wind speed showed a greater effect on the aerodynamic forces than predicted. The amplitude of the drag force under the pulsating wind became larger in a vehicle having a shape that experienced a large drag force under steady wind conditions. It is concluded that even under fluctuating wind conditions, there exists a critical angle of 30° at which the vehicle experiences either high or low fluid forces.

Keywords: Road vehicle; Fluctuating wind; Aerodynamic characteristics; Ahmed body, Wind-tunnel experiment.

1. INTRODUCTION

This study aimed at investigating the aerodynamic characteristics of a vehicle subjected to periodically fluctuating headwinds and clarifying the effect of the rear shape of the vehicle on these characteristics.

In recent years, the emphasis on conservation of the environment and reduction in energy consumption has significantly increased. In the automotive industry, research and development of vehicles with low flow resistance has become prevalent owing to the increased interest in the development of electric vehicles (EVs) (Kaneko, 2016). For this reason, wind-tunnel tests are conducted extensively. The wind tunnels employed in these experiments are becoming larger to test full-scale vehicles (Tadakuma *et al.*, 2015; Kato and Hashizume, 2015). Furthermore, they have evolved in type, from fixed to movable-floor wind tunnels (Takagi, 2012). Thus, wind-tunnel tests are often conducted under conditions close to real on-road conditions (Takagi, 2012; Sumida, 2017). However in most wind-tunnel experiments, measurements are taken at a constant airflow speed. Therefore, when

applying the results obtained in such a way to a real driving situation, it is necessary to consider changes in environmental conditions. Thus, flow situations in environmental conditions during real driving are determined beforehand, and a more fundamental investigation is required for the explication of aerodynamic characteristics (Tadakuma *et al.*, 2015).

Hucho and Sovran (1993) reviewed past studies on aerodynamics of road vehicles. In addition, Choi *et al.* (2014) explained recent research trends related to aerodynamic characteristics of large vehicles. In these papers, the importance of investigating the unsteady flow behavior around a vehicle body is advocated strongly. The same is emphasized by Fuller *et al.* (2013). However, the effect of ever-changing environmental conditions on aerodynamic characteristics remains undiscussed. Almost all studies have been conducted under conditions involving a constant driving speed or wind speed.

Nevertheless, as stated above, vehicles are frequently driven in natural wind conditions determined by atmospheric fluctuations. This causes a change in wind direction against the direction of vehicle movement, and the vehicles, in

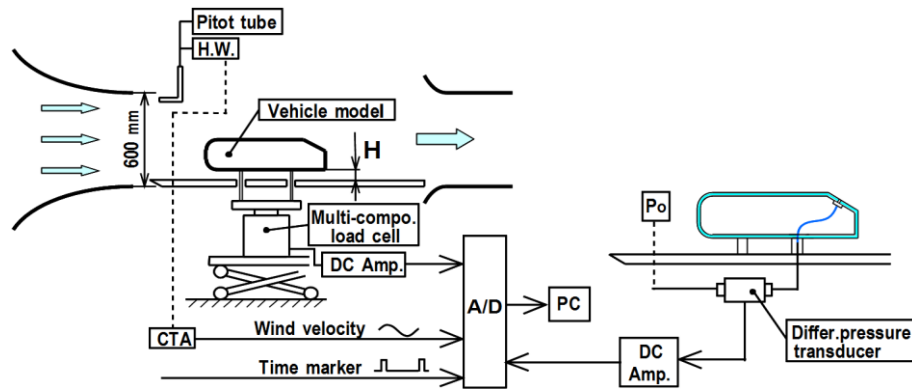


Fig. 1. Schematic of experimental setup and measurement system of fluid forces, wind speed, and pressure.

a sense, may be subjected to a fluctuating headwind. The aerodynamic characteristics under such a fluctuating wind condition are very important, particularly for large vehicles such as buses and trucks. The need for analyzing aerodynamic characteristics under not only conventional steady airflow conditions but also under fluctuating airflow conditions was emphasized by Wordley and Saunders (2008), Fuller *et al.* (2013), and Liu *et al.* (2016). When the test is conducted in a natural wind environment, the vehicle is under the influence of uncontrolled atmospheric fluctuations. Consequently, it becomes difficult to reproduce on-road conditions and compare data on natural winds and road conditions. For this reason, systematic studies are difficult to execute, and it seems that such studies have not been conducted yet. If a wind tunnel that can simulate environmental airflow is used, aerodynamic characteristics can be analyzed. Therefore, it will be possible to verify (Kato and Hashizume, 2015; Liu *et al.*, 2016; Wordley and Saunders, 2008; Fuller *et al.*, 2013) the correlation between results obtained under steady winds and in on-road experiments. This approach is widely applied in other areas (such as aircraft systems), with the aim of obtaining a valid aerodynamical model (Lichota *et al.*, 2017).

Sumida (2017) measured the fluid forces acting on a blunt-bodied vehicle (Ahmed *et al.*, 1984) under unsteady upstream flow conditions. In that test, an advanced wind tunnel (Sumida, 2017) that could drive its wind to fluctuate periodically was employed. They found that the fluid forces due to fluctuating winds were different from those at a constant wind speed (Sumida, 2017).

On the basis of the above fundamental findings, this study experimentally investigated the fluid forces acting on a vehicle under periodically fluctuating headwind conditions. In the experiment, we employed the Ahmed-type model (Ahmed *et al.*, 1984) as the test vehicle body. Furthermore, we addressed the problems related to vehicles driven at a constant speed but experiencing periodically fluctuating headwinds. In particular, we focused on the time-dependent fluid forces for the various rear

slant angles of the Ahmed-type vehicle model. The measurements of the drag and lift forces acting on the models and pressure distributions on the centerline of the models were obtained. Next, by comparing the obtained results with those under steady wind conditions, we determined the effects of the rear slant angle on the unsteady fluid forces. This work will help understand the effects of atmospheric wind fluctuations on aerodynamic characteristics of vehicles.

2. EXPERIMENTAL SETUP AND METHODS

2.1 Wind Tunnel

The experiments were conducted in the advanced wind tunnel at Kindai University's Research Institute of Fundamental Technology for the Next Generation (KURING) (Sumida, 2017). The schematic of the wind tunnel, experimental set up, and measurement system are shown in Fig. 1. The latter two components were newly constructed on the basis of the previous study (Sumida, 2017). The contraction ratio of the wind tunnel is 5.4:1, and the nozzle exit has a square cross-section of length 600 mm per side. In accordance with the experiment, the wind tunnel can be selectively set in three ways: as a closed-circuit wind tunnel, semi-open wind tunnel, or a single-circuit wind tunnel. Owing to the ease of executing measurements, we chose the semi-open type with the test section being open.

The periodically fluctuating wind was generated using an axial flow blower consisting of 14 blades and driven by a 45 kW electric motor. The rated air volume and rotational speed are 900 m³/min and 1755 rpm, respectively. Varying wind speeds could be obtained by adjusting the maximum and minimum pitch angles of the rotor blades and setting the interval time of the pitching motion. This setting is programmable.

This study aimed at analyzing specific aerodynamic characteristics under fluctuating headwinds and comparing them with those under steady winds. Therefore, although the wind-tunnel facility in

KURING is equipped with a boundary-layer suction device, it was not used because it is difficult to control under fluctuating wind conditions.

2.2 Test Vehicle Model

The vehicle model employed in the experiment was the Ahmed-type model (Ahmed *et al.*, 1984), shown in Fig. 2, to compare our results with those hitherto obtained under steady wind conditions (Ahmed *et al.*, 1984; Banga *et al.*, 2015). The test model is a 1/2.5-scale Ahmed model (Ahmed *et al.*, 1984) and is therefore approximately 1/12.5 of a practical vehicle. The dimensions are length (ℓ) = 417.6 mm, width (b) = 155.6 mm, and height (h) = 115.2 mm. The section measuring 76.9 mm in the rear part of the model can be adjusted at a slant angle, θ , ranging from 0 to 40°.

2.3 Experimental Setup and Measurement Procedures

The measurement system is comprised of three parts for measuring the wind speed, aerodynamic force, and pressure (Fig. 1). The velocity of the airflow issued from the wind-tunnel's nozzle exit was measured using a hot-wire anemometer and Pitot tube. The degree of turbulence at the nozzle exit was less than 0.7% when the wind speed ranged from $V=10\text{--}20$ m/s. The model was supported by four columns of diameter 8 mm, which were fitted to the multicomponent load cell (Nissho-Electric-Works Co.: LMC-3502). The installation height H of the model could be changed in the range of 15 to 40 mm. Thereby, the drag, lift, and side components (D , L , and S , respectively) of the resultant fluid force F acting on the vehicle model could be detected. The pressure distribution on the centerline of the vehicle was measured using a differential pressure transducer (JTEKT: DD101K) as shown in Fig. 1. Measurement holes of diameter 1.5 mm were installed around the model at 40 positions or more. The reference pressure p_0 is the static pressure measured by a Pitot tube located on the top left of the model in the free stream flow, as shown in Fig. 1.

The output voltages of the load cell and pressure transducer were suitably amplified using direct current amplifiers (Nissho-Electric-Works Co.: DSA-100A, and JTEKT: AA3004, respectively). Next, they were converted into digital values through a data acquisition system (Keyence: NR-500), being recorded in a personal computer. At the same time, the time marker signal indicating the position of the pitch angle of the rotor blade was also recorded, as shown in Fig. 1. Data were recorded for approximately 20 fluctuation cycles and sampled for approximately 30 to 120 s.

Data acquisition accuracy was taken into account for measurements of unsteady fluid forces and pressures. The parallelism setting of the model with respect to the flow issued from the nozzle exit was checked by measuring the side force in the steady flow. The side force S was 1.3% of the drag force D or less. It was estimated that the accuracy of flow angle of the model was within 0.2°. The errors in

the flow angle showed that errors in the free-stream dynamic pressure are 1 %, at the most, in the pressure measured. The accuracies of the instruments measuring force and pressure were less than 0.2 and 0.4%, respectively, with respect to their full-scale values. Moreover, the characteristic frequencies of the multicomponent load cell were 170 Hz in the wind direction and 130 Hz in the vertical and lateral directions. The pressure transducers had a characteristic frequency of not less than 3 kHz. The frequency response characteristics were very high compared to an effectuated cycle of 1/1.5 Hz of a pulsating wind. The data acquisition system was calibrated, as necessary, before the experiments and used. In addition, when the measurements were made, the outputs from the instruments were passed through a low-pass filter of 20 Hz.

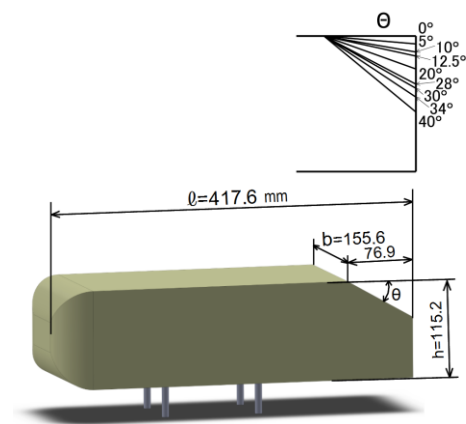


Fig. 2. Ahmed-type vehicle model with various slant angles.

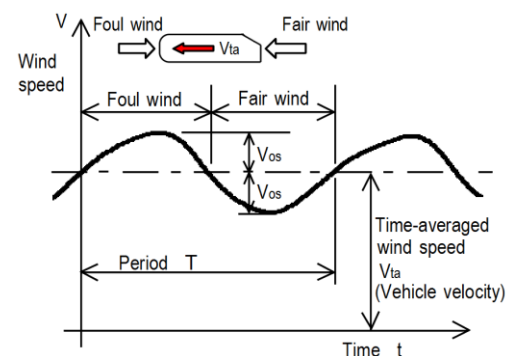


Fig. 3. Descriptive diagram of wind configuration.

2.4 Experimental Conditions

The experiments were mostly carried out at a time-averaged wind speed of $V_{ta} = 13.0 \pm 0.15$ m/s, as mentioned in Table 1. Here, the subscripts ta and os indicate time-mean and amplitude values, respectively. These conditions were chosen on the basis of the previous work (Sumida, 2017). The wind configuration is shown in Fig. 3. This speed

Table 1 Experimental conditions in pulsating wind

Fluctuation period T s.	Time-averaged wind speed $V_{ta} \pm 0.15$ m/s	Fluctuation wind speed $V_{os} \pm 0.06$ m/s	Amplitude ratio $\eta = V_{os}/V_{ta}$
1.5	13.0	2.63	0.202
2.0	13.1	2.58	0.197
3.0	12.6	2.90	0.230
5.0	14.2	2.40	0.169

gives the value of Reynolds number, Re , as 3.59×10^5 , where $Re = V_{ta} \ell / \nu$, and ν is the kinetic viscosity of the air. The conditions are given in the table: $T = 1.5\text{--}5.0$ s for the fluctuation period and $V_{os} = (2.40\text{--}2.90) \pm 0.06$ m/s for the velocity fluctuation, given the amplitude ratio $\eta = V_{os} / V_{ta} \approx 0.169\text{--}0.230$.

3. RESULTS AND DISCUSSION

In the wind-tunnel test using a vehicle model, it is necessary to prior examine the effects of parameters such as the blockage ratio and height from the ground plane on the results (Flow Technology Expert Committee, Wind-Tunnel Correlation Working Group, 1998; Hucho and Sovran, 1993). The blockage ratio in the experiment was less than 1/20 at which there was no effect of the blockage ratio (Hucho and Sovran, 1993; Society of Automotive Engineers of Japan Editorial Board, 2004). The thickness of the boundary layer (Wang et al., 2006) was approximately 8 mm at 285 mm measured from the leading edge of the ground plane, at which the vehicle model is placed, at a free airflow velocity of 13 m/s.

3.1 Fluid Forces in Wind with no Fluctuation and Preliminary Examination

The fluid forces acting on the vehicles were decomposed into the drag and lift forces, D and L , respectively. Both components were normalized using the dynamic pressure $\rho V^2/2$ and projected frontal area A of the vehicle model per the following equation, with ρ being the air density.

$$\left. \begin{aligned} C_D &= D/(\rho V^2 A/2), \\ C_L &= L/(\rho V^2 A/2). \end{aligned} \right\} \quad (1)$$

Thus, the fluid forces were evaluated using the non-dimensional coefficients of C_D and C_L .

3.1.1 Preliminary Measurements

The flow field around the vehicle model is slightly dependent on the structure of the testing part of the wind tunnel (Hausmann et al., 1988; Wickern, 2007). This influences the aerodynamic performance. We performed a preliminary analysis on the influences of the ground-plane length and supporting-column height on the aerodynamic forces acting on the vehicle models.

For the former, it was confirmed that there is no

influence of the ground-plane length, x_e , measured from the model's rear end, on the fluid force when x_e is larger than 600 mm, i.e., $x_e/\ell > 1.4$. Thereafter, we performed the experiments with a length x_e of approximately 1200 mm.

Subsequently, the influence of the supporting columns on the fluid forces in the model was examined. The drag force of the columns increased in proportion to the installation height H of the model, and the coefficient of the columns increased slightly with an increase in the wind speed V . On the other hand, the drag coefficient C_D of the model gradually decreased as V increased. However, when the wind speed V exceeded 10 m/s, the dependency of the coefficients on V cannot be seen gradually. For $H = 40$ mm, the drag force of the columns corresponded to approximately 15–18% of that of the model, when $V = 10\text{--}20$ m/s. On the other hand, the lift force of only the supporting columns was very small compared to that of the model, and the value remained unchanged for a height H of 20–40 mm. Therefore, the corresponding illustrations are omitted.

In wind-tunnel tests (Minguez et al., 2008; Meile et al., 2011; Wang et al., 2013; Banga et al., 2015; Volpe et al., 2015; Keogh et al., 2016; Thacker et al., 2013) and a water-channel test (Tunay et al., 2013) previously conducted with Ahmed-type vehicle models, measurements were obtained at $H = 0.174h$, with a set up geometrically similar to that in the experiment conducted by Ahmed et al. (1984). However, the problem regarding the formation of a boundary layer on the ground plane and its effect on the fluid forces have not been discussed concretely in these works. Therefore, we executed our experiments at $H = 40$ mm ($= 0.347h$) to minimize the influence of the boundary layer formed on the ground plane.

3.1.2 Fluid Forces under Steady Wind

Drag and Lift Coefficients, C_D and C_L

Figures 4 and 5 show the relationship between C_D and C_L , respectively, and the rear slant angle θ of the model when $V = 13$ m/s ($Re = 3.59 \times 10^5$). The results show that the dependency of C_D and C_L on θ is similar to those experimentally found at $Re = 4.29 \times 10^6$ by Ahmed et al. (1984) and numerically obtained at $Re = 1.04 \times 10^7$ by Banga et al. (2015). However, in the latter, the angle of 30° or less is the object of comparison.

That is, although the drag coefficient C_D takes a lower value at $\theta = 10^\circ$, it increases rapidly when θ becomes larger than 20° , reaching the maximum value at $\theta = 30^\circ$ (Fig. 4). However, when θ remains the same (30°), the value of C_D decreases and takes a different lower value. Once the flow is in a state with a high or a low value, the transition to the other state happens rarely. The transition to the state with a high value from the state with a low value, in

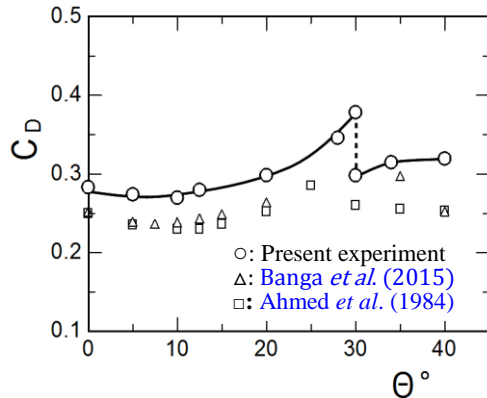


Fig. 4. Relationship between drag coefficient C_D and rear slant angle θ under steady wind conditions ($V=13$ m/s).

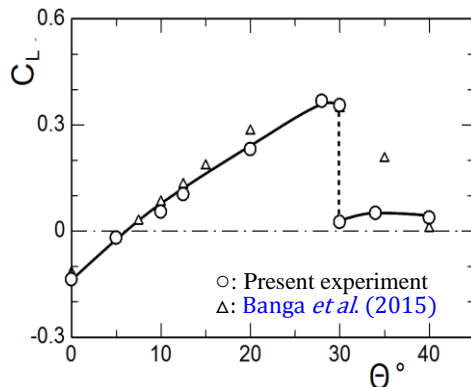


Fig. 5. Relationship between lift coefficient C_L and rear slant angle θ under steady wind conditions ($V=13$ m/s).

a general sense, seems to readily occur in terms of percentage.

On the other hand, the lift coefficient C_L increases as θ increases, and at $\theta = 30^\circ$, it simply takes a high or a low value in accordance with the value of C_D , as shown in Fig. 5. However, when θ exceeds 30° , C_L takes a low value close to the case of $\theta = 0^\circ$, and the change in C_L with θ becomes small. The reason is as follows. For the case of $\theta > 30^\circ$, the slant angle steepens, and the vehicle resembles the rear shape at $\theta = 0^\circ$. Therefore, it appears that the vehicles with $\theta = 0^\circ$ and $\theta > 30^\circ$ are subjected to fluid forces owing to a similar flow state.

Although [Banga et al. \(2015\)](#) performed a

computational fluid dynamics (CFD) analysis of the vehicles with $\theta = 0-40^\circ$; however, the values of C_D and C_L for slant angles larger than the critical angle were not calculated. According to them, it is because beyond 30° , flow separation occurs, and C_D and C_L become randomly dispersed.

Transition of Fluid Forces for Model with $\theta = 30^\circ$

As has been noted, the fluid force acting on Ahmed-type vehicles drastically changes at a slant angle 30° , which is the critical angle. This paper briefly gives additional explanations. Recently, such a flow was extensively examined for two typical cases of $\theta = 25^\circ$ and $\theta = 35^\circ$, with a high and a low force, respectively. There are many works, namely [Tunay et al. \(2013\)](#), [Minguez et al. \(2008\)](#), [Aljure et al. \(2014\)](#), [Lehmkuhl et al. \(2012\)](#), [Venning et al. \(2015\)](#) for $\theta = 25^\circ$, and [Banga et al. \(2015\)](#) and [Wang et al. \(2013\)](#) for $\theta = 35^\circ$. In these studies, flow fields around the vehicle were investigated using particle image velocimetry (PIV) ([Wang et al., 2013](#); [Venning et al., 2015](#); [Volpe et al., 2015](#); [Thacker et al., 2013](#); [Tunay et al., 2013](#)) and CFD techniques ([Banga et al., 2015](#); [Meile et al., 2011](#); [Minguez et al., 2008](#); [Aljure et al., 2014](#); [Lehmkuhl et al., 2012](#); [Tunay et al., 2013](#)). However, their works only provide results obtained for a specific value of θ . Therefore, a clear explanation concerning the transition mechanism is not available ([Banga et al., 2015](#); [Wang et al., 2013](#); [Thacker et al., 2013](#)). This problem remains unsolved.

Considering these situations, we examined how a disturbance locally induced by a circular cylinder affected the occurrence of the transition in fluid forces. Circular cylinders with diameters d of 8, 12, and 15 mm were installed at a position 287 mm from the tip of the model, as shown in Fig. 6. For example, the transition phenomenon for $d = 8$ mm occurred at $h_c = \pm h/2$. Furthermore, when the diameter of the cylinder was 12 mm, the transition occurred only at $h_c = +h/2$. Fluid forces for $h_c = 0$ and $-h/2$ took only the high and low value, respectively. Although the results are interesting, we are unable to explain the reasons for these results at this point.

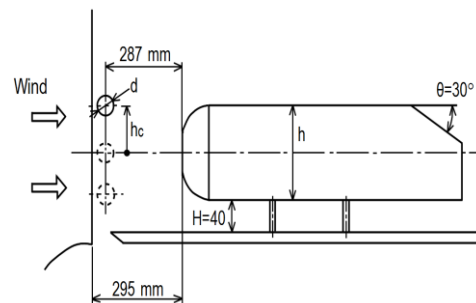


Fig. 6. Setup for examination of disturbance induced by a circular cylinder on fluid force transition.

3.2 Fluid Forces under Fluctuating Headwind

In this study, we addressed the flow problem in which a vehicle is running at a fixed speed under wind fluctuations occurring alternately in the traveling and adverse directions, as demonstrated in Fig. 3. That is, the fluctuating wind that a running vehicle receives from the front (headwind) is modeled as a pulsating wind in a wind-tunnel test. Such a fluctuating headwind is expressed in terms of the fluctuation speed and period of fluctuation. Moreover, it is considered that effects of the fluctuation on the aerodynamic force will differ according to the speed of the running vehicle. Therefore, it can be said that the aerodynamic force characteristics of the vehicle, subjected to pulsating winds, depend roughly on the amplitude ratio of the fluctuating wind speed to the speed of the traveling vehicle (time-averaged wind speed) and on fluctuation period. Nevertheless, it is not easy to perform tests under these wind conditions.

3.2.1 Influence of Fluctuation Frequency on Fluid Forces

First, we will discuss the effects of the fluctuation period on the aerodynamic forces. Figure 7 shows changes in the drag and lift forces with time for the model with $\theta = 20^\circ$ under several fluctuation periods, for which the experimental conditions are mentioned in Table 1. The relationships between the fluid forces and wind velocity for a cycle are illustrated in Fig. 7, in the form of a Lissajous diagram. Here, the wind velocity changes almost sinusoidally with time t as illustrated later (see Fig. 8). For a fluctuation period T of 5 s, there is little difference in the fluid forces of D and L in the increasing and decreasing phases of the wind velocity. The change in these forces with time is not quasi-steady even at $T = 5$ s. Moreover, for a fluctuation period of 3 s or less, the influence of the fluctuation of the wind becomes remarkable. For instance, even if the instantaneous wind velocity is the same in a cycle, the airflow causes stronger forces at the increasing phase compared to those at the decreasing phase.

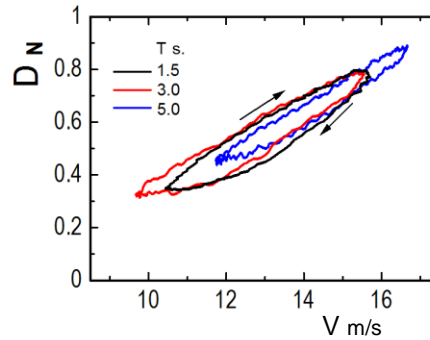
Thus, in this paper, we describe the results obtained for fluctuation period of $T = 1.5$ s, at which the wind fluctuation has the strongest influence on the aerodynamic forces. Now, we will discuss the effect of the slant angle θ on the fluid forces.

3.2.2 Influence of Slant Angle on Fluid Forces

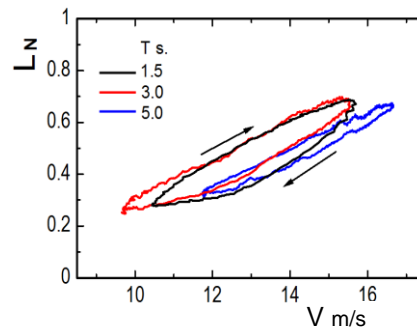
Figure 8 shows the results obtained for models with different slant angles under pulsating winds. The time mean and amplitude of the wind velocity are $V_{ta} = 13.0 \pm 0.15$ m/s and $V_{os} = 2.63 \pm 0.06$ m/s, respectively, with a pulsation (fluctuation) period of $T = 1.5$ s, as provided in Table 1. This gives the amplitude ratio of $\eta = V_{os}/V_{ta} = 0.202$. In Fig. 8, the changes in D , L , and wind velocity $V(t)$ with time are illustrated. Here, the abscissa is the phase angle Θ , which is described later in Eq. (2). The dashed and dotted lines show the time-mean values, and

velocity V is nondimensionalized by the time-averaged value V_{ta} . It can be seen from Fig. 8 that the wind velocity changes almost sinusoidally with time t and can be simply expressed using the following equation:

$$V(\Theta) \approx V_{ta} + V_{os} \cdot \sin \Theta, \quad (2)$$



(a) Drag force.



(b) Lift force.

Fig. 7. Effect of pulsation frequency on fluid forces ($\theta = 20^\circ$). Detailed experimental conditions are given in Table 1.

where $\Theta (= \omega t)$ is the phase angle and ω is the pulsation frequency.

The time-averaged drag force D_{ta} in each model is slightly larger than the drag force under a steady wind with the same value as the time-averaged velocity of the pulsating wind. The details are described later. Moreover, the fluctuating component of the drag force, D_{os} , is more than 40% of the time-averaged value D_{ta} , though the amplitude ratio η is 0.202. Furthermore, the drag force varies with a phase lead from the wind fluctuation. The higher the drag force on the model under steady wind conditions, the larger is the phase difference ϕ_D between D and V under pulsating wind conditions. When the slant angle exceeds 20° , the phase difference ϕ_D reaches 16° . In particular, it is a noteworthy result, shown in Fig. 8(c); both high and low fluid forces evidently occur when the slant angle is 30° , the critical angle under steady wind conditions. At a slant angle of 30° , the model experiences the transition phenomenon of fluid forces even when the wind has not only a local turbulence but also a fluctuation of $\eta = 0.202$. The

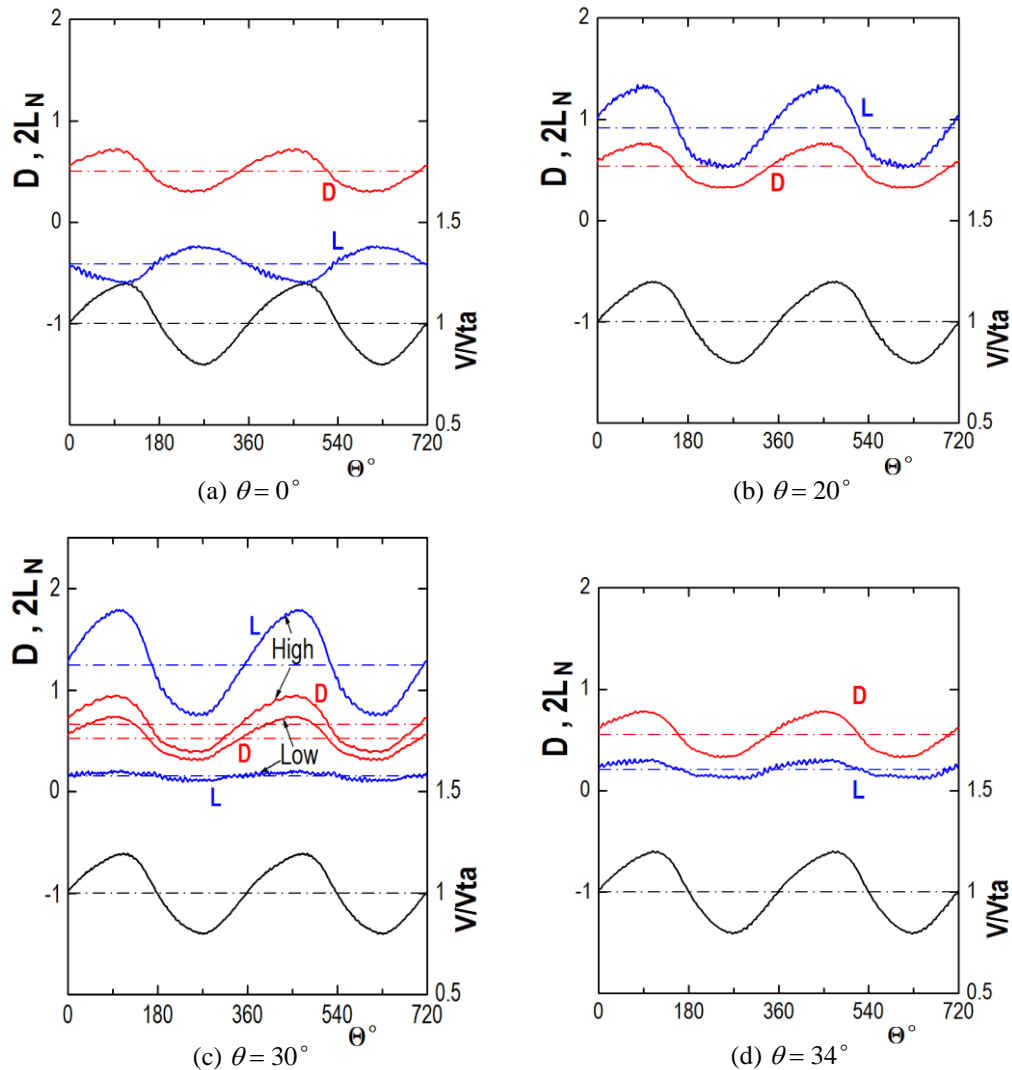


Fig. 8. Changes in drag and lift forces with time under pulsating wind conditions with period $T = 1.5$ s. Dashed and dotted lines denote time-mean values, D_{ta} and L_{ta} , respectively.

transition phenomenon appears to depend on the state of starting operation of the wind tunnel for the pulsating wind. For this reason, the transition did not appear while measuring the forces. This issue is arousing the interest of specialized scholars: there appears a transition phenomenon even in an upstream flow with a fluctuation of $\eta = 0.202$. This should be noted while actually driving on the road.

On the other hand, the change in the lift force L with time against the wind fluctuation differs considerably while depending on the slant angle. In Fig. 8(a), for a model with symmetric upper and lower halves at $\theta = 0^\circ$, the lift force changes in the opposite phase of the fluctuating wind. In this model, the lift force shows negative values through a cycle because the pressure decrease on the floor side is larger than that on the roof side. Conversely, in models with a slant rear shape, the pressure on

the slant surface decreases as the slant angle increases (refer to Fig. 9), causing the lift force to increase in the upward direction (positive values). As a result, the lift force changes in proportion with the increase and decrease in the wind velocity. At a critical angle of 30° , the lift force takes either a high or low value in accordance with the value of the drag force [Fig. 8(c)]. For the low value, the amplitude of L becomes smaller compared to the cases of other slant angles. In addition, for models with $\theta > 30^\circ$, the fluctuations of L are noticeably small [Fig. 8(d)]. The amplitude ratio of the lift force, L_{os}/L_{ta} , exceeds 0.4, as calculated from Figs. 8(a) and (b), except when the drag force at $\theta = 30^\circ$ takes a low value. The drag and lift forces act on the vehicles at two or more times the amplitude ratio of the wind speed. Therefore, the fluctuation of the wind speed has a higher effect on vehicles than was generally thought.

3.2.3 Changes in Static Pressure on Body Surface with Time

Figure 9 shows variations in static pressures at representative positions, which are on the centerline of the model surface, with time. The abscissa is the phase angle θ . In the figure, the static pressure p is displayed in the form of the pressure coefficient C_p defined by the following expression:

$$C_p = (p - p_o) / (\rho V_{ia}^2 / 2). \quad (3)$$

Here, p_o is the reference pressure that is the static pressure in the wind tunnel measured by the Pitot tube (refer to Fig. 1). Moreover, the positions at which the illustrated pressures were measured are concretely indicated in the upper part of the figure.

The drag force varies principally owing to the change in the pressure on the front surface. This pressure (F_6) varies periodically with a phase lead of approximately 15° from the wind fluctuation. The pressure coefficient C_p at F_6 is in the range of 1.52 to 0.66 and rises rapidly when the headwind becomes strong. The drop in pressure on the nose part of the front (F_1 and F_{11}) varies with a slight phase delay from the wind fluctuation. The pressure drop in the nose part is slightly large at the floor side (F_{11}) compared to that at the roof side (F_1). In addition, although C_p on the floor and roof sides takes negative values, the absolute value of the former (L_4) is slightly larger than that of the latter (U_4), which is not illustrated in Fig. 9. On the other hand, C_p on the rear surface changes in the opposite phase to that on the front surface, and it takes values ranging from -0.1 to -0.5 . Further, the negative pressure on the slant surface increases with an increase in θ , and it reaches the maximum at $\theta = 30^\circ$. This causes an increase in the drag and lift forces, particularly for the case of $\theta > 20^\circ$. However, when θ exceeds 30° , the pressure at R_1 is analogous to that at R_6 with $\theta = 0^\circ$.

3.2.4 Influence of Slant Angle on Time-Averaged Fluid Forces

Henceforth, we express the fluid forces as dimensionless quantities, and move forward with the examination. The drag and lift forces, D and L , were normalized using the dynamic pressure, $\rho V_{ia}^2 / 2$, and the time-averaged velocity, V_{ia} , of the wind. They are expressed in the same manner as Eq. (1):

$$\left. \begin{aligned} C_D(t) &= D(t) / (\rho V_{ia}^2 A / 2), \\ C_L(t) &= L(t) / (\rho V_{ia}^2 A / 2). \end{aligned} \right\} \quad (4)$$

First, we compared the time-mean values of the drag and lift forces, $C_{D,ta}$ and $C_{L,ta}$, respectively, with the values under steady wind conditions. The results for $C_{D,ta}$ and $C_{L,ta}$ are shown in Figs. 10 and 11, respectively. The time-averaged drag coefficients $C_{D,ta}$ at every slant angle are slightly higher by approximately 3 to 7% compared to those under steady wind conditions (Fig. 10). Accordingly, the power loss corresponding to the increment of the fluid force appears when vehicles are subjected to a fluctuating headwind.

On the other hand, for the lift coefficient, there is a discernible difference in terms of the slant angle, as shown in Fig. 11. The degree of increase in $C_{L,ta}$ due to wind fluctuation is considerably high for models with $\theta \geq 30^\circ$, which take a low resistance. Furthermore, it seems that the lift force is more sensitive than the drag force to wind fluctuations.

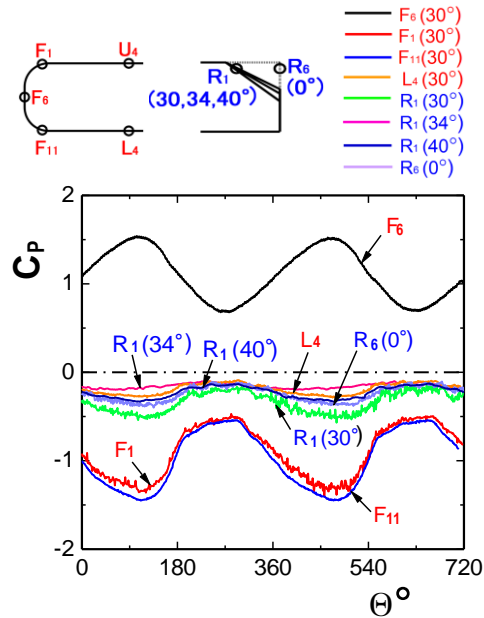


Fig. 9. Changes in wall static pressure on body surface with time at several locations.

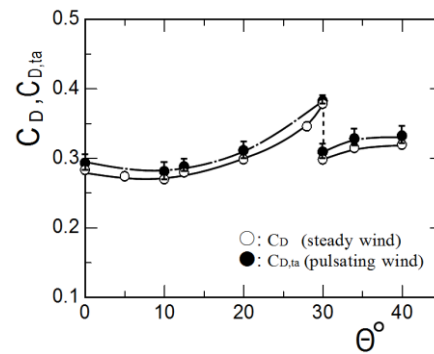


Fig. 10. Comparison of time-averaged $C_{D,ta}$ with C_D under steady wind conditions.

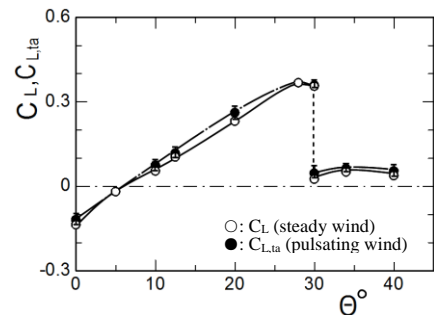


Fig. 11. Comparison of time-averaged $C_{L,ta}$ with C_L under steady wind conditions.

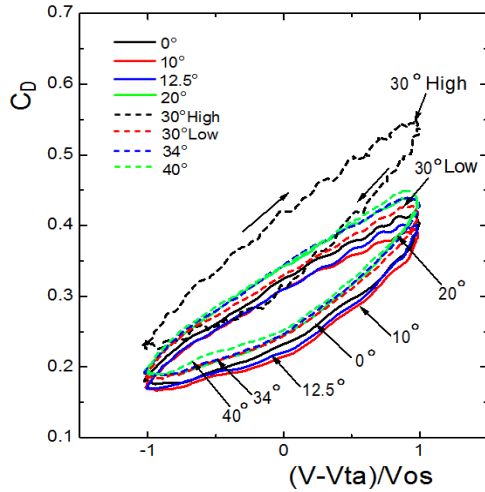


Fig. 12. Lissajous diagram of C_D under pulsating wind conditions with $T = 1.5$ s.

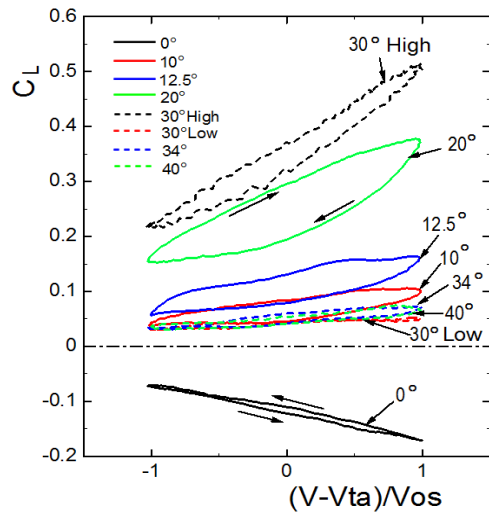
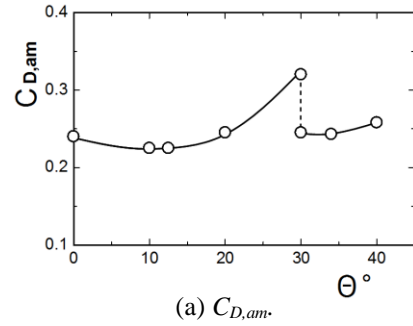


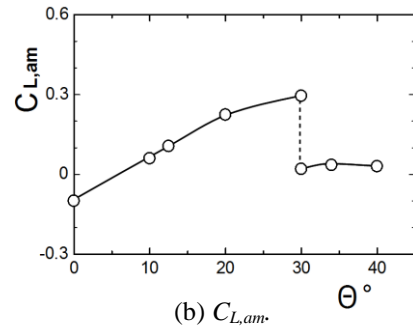
Fig. 13. Lissajous diagram of C_L under pulsating wind conditions with $T = 1.5$ s.

3.2.5 Lissajous Diagrams of C_D and C_L

Next, we discuss the fluid forces arising from the wind fluctuation in more detail. For this, the relationships between the fluid forces and wind velocity for a cycle are shown in the form of Lissajous diagrams in Figs. 12 and 13. Moreover, Fig. 14 shows the differences, $C_{D,am}$ and $C_{L,am}$, between the maximum and minimum values of C_D and C_L , respectively, during a cycle. In addition, the differences in C_D and C_L values at the time when $(V-V_{ta})$ both in the acceleration and deceleration terms become 0 m/s, are shown in Fig. 15. The differences are denoted by $C_{D,dif}$ and $C_{L,dif}$, respectively. They indicate the degree of the phase difference between the force and wind speed under pulsating wind conditions. That is, an increase in their values shows that the phase lead becomes large. In addition, a negative value indicates that the force changes in the opposite phase to the wind speed, as seen from the results at $\theta = 0^\circ$ in Figs. 13 and 15.

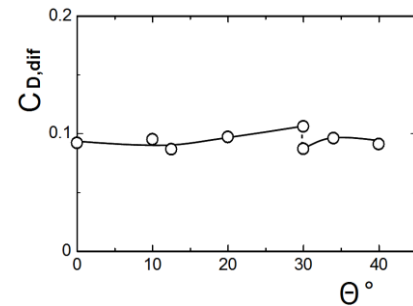


(a) $C_{D,am}$.

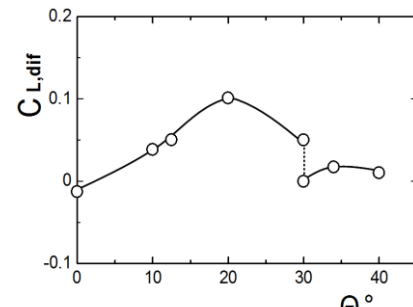


(b) $C_{L,am}$.

Fig. 14. Influence of slant angle θ on $C_{D,am}$ and $C_{L,am}$ under pulsating wind conditions with $T = 1.5$ s.



(a) $C_{D,dif}$.

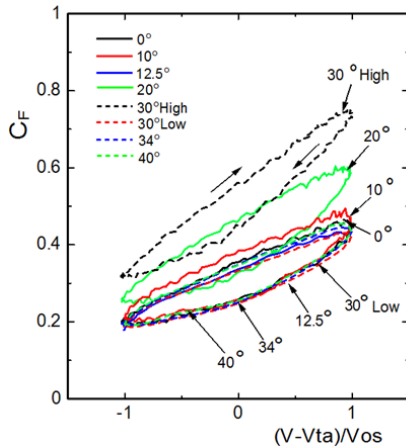


(b) $C_{L,dif}$.

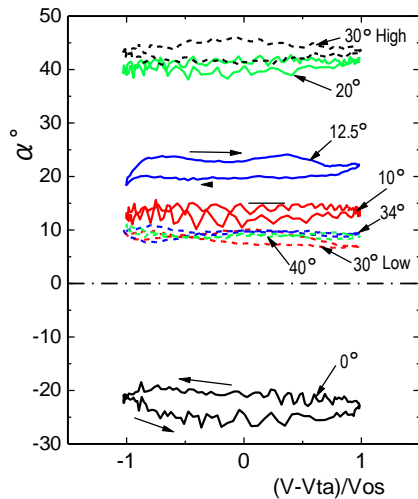
Fig. 15. Influence of slant angle θ on $C_{D,dif}$ and $C_{L,dif}$ under pulsating wind conditions with $T = 1.5$ s.

In Figs. 12 and 13, C_D and C_L change with time in a clockwise direction, except for C_L at $\theta = 0^\circ$. C_D increases approximately in proportion to the wind speed when the headwind becomes strong. In contrast, it decreases rapidly for the first half of the phase when the wind weakens. The relationship

between $C_{D,am}$ and θ [Fig. 14(a)] is similar to the relationship of C_D and θ under steady wind conditions (Fig. 4). The value of $C_{D,am}$ ranges from 0.21 to 0.32, and these values correspond to approximately 80% of the C_D values under a steady wind. $C_{D,dif}$ is small at $\theta \approx 10^\circ$ and slightly increases when θ approaches the value of 30° [Fig. 15(a)].



(a) Resultant force coefficient, C_F .



(b) Acting direction of resultant force, α .

Fig. 16. Resultant force coefficient C_F and its direction α under pulsating wind conditions with $T = 1.5$ s.

However, it takes the lowest value at $\theta = 30^\circ$ with a low fluid resistance. Predominantly, the value of $C_{D,dif}$ is equivalent to one-third of the C_D value under a steady wind.

On the other hand, the lift coefficient C_L differs extremely as the slant angle θ changes (Fig. 13). In particular, for the model with $\theta = 0^\circ$ with symmetry between the upper and lower halves, the lift force acts downward for a cycle, and its magnitude is almost proportional to the increase and decrease in the wind, as shown in Fig. 13. The slant-angle dependency of $C_{L,am}$ is similar to that of C_L under a

steady wind; further, the value of $C_{L,am}$ is almost the same as that of C_L under a steady wind [Fig.14 (b)]. Nevertheless, the value of $C_{L,dif}$ is the largest for the model with $\theta = 20^\circ$, whereas there is little difference for the models with $\theta \geq 30^\circ$, indicating a low C_L [Fig. 15(b)].

3.2.6 Resultant Force Coefficient and Direction of Its Action

In Fig. 16, the resultant force F and its direction α acting on models are shown, in which F is nondimensionalized in the same manner as Eq. (4), i.e.,

$$C_F(t) = F(t)/(\rho V_{ta}^2 A/2). \quad (5)$$

Here, $F(t) = [D(t)^2 + L(t)^2]^{1/2}$, and the direction is obtained from $\alpha = \tan^{-1}[L(t)/D(t)]$.

The C_F values in the Lissajous diagrams illustrated for each model change clockwise with respect to time, except for α at $\theta = 0^\circ$. The resultant force F for models with $\theta = 0^\circ$ acts in the direction of α , ranging from -20 to -25° . It starts to act upward as θ increases. C_F rapidly increases in the range of $\theta = 12.5$ to 30° , starting to act in the direction corresponding to approximately 44° . However, when the slant angle exceeds the critical angle of 30° , the direction of F does not change much with θ and time, and F acts in the direction corresponding to approximately 8° .

4. CONCLUSIONS

Wind-tunnel experiments were performed to study the aerodynamics of an Ahmed-body vehicle subjected to fluctuating headwinds. The effects of the slant angle on the fluid forces were investigated. The principal findings are summarized as follows.

- (1) Unsteady upstream flows exert significant effects on the fluid forces, and the aerodynamic characteristics are dependent on the slant angle of the vehicle's rear shape. Furthermore, there exist unsteady effects persistently even under a fluctuating wind with a period of period 5 s.
- (2) The larger the drag force on the model under a steady wind with no fluctuation, the larger is the variation in the drag force during a cycle. The fluctuation of the fluid forces corresponds to approximately twice that of the amplitude ratio of the wind velocity. The time-mean value of the drag force is 3 to 7% higher than that under a steady wind.
- (3) The difference between the lift forces at the times when the wind speed in the acceleration and deceleration terms becomes equal to the time-averaged speed reaches as much as 40% of the lift force under a steady wind; it is the largest for the model with $\theta = 20^\circ$.
- (4) Under a fluctuating wind, the vehicles receive the resultant force, the variation of which corresponds to almost that under a steady wind during a cycle. The force increases in the range of $\theta = 12.5$ to 30° , whereas it does not change

much for $\theta > 30^\circ$.

- (5) For models with a slant angle of 30° , the vehicle experiences either of the high or low fluid forces in the same manner as in the case of a steady wind. The angle corresponds to the critical angle even when the wind shows a large fluctuation.

ACKNOWLEDGEMENTS

We wish to thank Mr. Seiya Morita, a student in our laboratory who participated in designing the experimental apparatus and conduction of the experiment. Moreover, we are grateful to the MEXT-Supported Program of the Strategic Research Foundation at Private Universities (Grant No. S0901045) for the support in this research.

REFERENCES

- Ahmed, S. R., G. Ramm and G. Faltin (1984). Some salient features of the time-averaged ground vehicle wake. *SAE Paper* 840300.
- Aljure, D. E., O. Lehmkuhl, I. Rodriguez and A. Oliva (2014). Flow and turbulent structures around simplified car model. *Computers & Fluids* 96, 122-135.
- Banga, S., Md. Zunaid, N. A. Ansari, S. Sharma and R. S. Dugriyal (2015). CFD simulation of flow around external vehicle: Ahmed body. *IOSR Journal of Mechanical and Civil Engineering* 12(4), 87-94.
- Choi, H., J. Lee and H. Park (2014). Aerodynamics of heavy vehicles. *Annual Review of Fluid Mechanics* 46, 441-468.
- Flow Technology Expert Committee, Wind-Tunnel Correlation Working Group, eds. (1998). Testing correlation between wind tunnels for model automobile, *Society of Automotive Engineers of Japan*, Tokyo, Japan 1.
- Fuller, J., M. Best, N. Garret and M. Passmore (2013). The importance of unsteady aerodynamics to road vehicle dynamics. *Journal of Wind Engineering and Industrial Aerodynamics* 117, 1-10.
- Hausmann, F. K. S. and J. D. Vagt (1988). Influence of test-section length and collector area on measurements in 3/4-open-jet wind tunnels. *SAE Paper* 880251.
- Hucho, W. -H. and G. Sovran (1993). Aerodynamics of road vehicles. *Annual Review of Fluid Mechanics* 25, 485-537.
- Kaneko, M. (2016). Wind tunnel technologies for automobile development, *Journal of the Visualization Society of Japan*. 32 (124), 9-13.
- Kato, D. and Y. Hashizume (2015). Comparative method of vehicle aerodynamics between full-scale wind tunnel tests and on-road tests. *Journal of Society of Automotive Engineers of Japan* 69(7), 111-116.
- Keogh, J., T. Barber, S. Diasinos and G. Doig (2016). The aerodynamic effects on a cornering Ahmed body. *Journal of Wind Engineering and Industrial Aerodynamics* 154, 34-46.
- Lehmkuhl, O., R. Borrell, I. Rodriguez, C. D. Perez-Segarra and A. Oliva (2012). Assesment of the symmetry-preserving regularization model on complex flows using unstructured grids. *Computers & Fluids* 60, 108-116.
- Lichota, P., K. Sibilski and P. Ohme (2017). D-optimal simultaneous multistep excitations for aircraft parameter estimation. *Journal of Aircraft* 54(2), 747-758.
- Liu, X., Y. Han, C. S. Cai, M. Levitan and D. Nikitopoulos (2016). Wind tunnel tests for mean wind loads on road vehicles. *Journal of Wind Engineering and Industrial Aerodynamics* 150, 15-21.
- Meile, W., G. Brenn, A. Reppenhagen, B. Lechner and A. Fuchs (2011). Experiments and numerical simulations on the aerodynamics of the Ahmed body. *CFD Letters* 3(1), 32-39.
- Minguez, M., R. Pasquetti and E. Serre (2008). High-order large-eddy simulation of flow over the "Ahmed body" car model. *Physics of Fluids* 20, 095101.
- Society of Automotive Engineers of Japan Editorial Board, ed. (2004). Automotive Engineering Handbook, *Society of Automotive Engineers of Japan*, Tokyo, Japan.
- Sumida, M. (2017). KURING wind tunnel; Aerodynamic characteristics tests of road vehicles in time-dependent winds. *WSEAS Trans. Fluid Mechanics* 12, 53-57.
- Tadakuma, K., Y. Haramoto, T. Murayama and K. Maeda (2015). Development of full-scale wind tunnel to enhance aerodynamic and aero-acoustic performance. *Journal of Society of Automotive Engineers of Japan* 69(7), 104-110.
- Takagi, M. (2012). Automotive wind tunnels. *Journal of the Visualization Society of Japan*. 32(124), 9-13.
- Thacker, A., S. Aubrun, A. Leroy and P. Devinant (2013). Experimental characterization of flow unsteadiness in the centerline plane of an Ahmed body rear slant. *Experiments in Fluids* 54, 1479.
- Tunay, T., B. Sahin and H. Akilli (2013). Experimental and numerical studies of the flow around the Ahmed body. *Wind and Structures* 17(5), 515-535.
- Venning, J., D. Lo. Jacono, D. Burton, M. Thompson and J. Sheridan (2015). The effect of aspect ratio on the wake of the Ahmed body. *Experiments in Fluids* 56, 126.

- Volpe, R., P. Devinant and A. Kourta (2015). Experimental characterization of the unsteady natural wake of the full-scale square back Ahmed body: flow bi-stability and spectral analysis. *Experiments in Fluids* 56, 99.
- Wang, H. F., Y. Zhou, C. K. Chan and K. S. Lam (2006). Effect of initial conditions on interaction between a boundary layer and a wall-mounted finite-length cylinder wake. *Physics of Fluids* 18, 065106.
- Wang, X. W., Y. Zhou, Y. F. Pin and T. L. Chan (2013). Turbulent near wake of an Ahmed vehicle model. *Experiments in Fluids* 54, 1490.
- Wickern, G. (2007). Recent literature on wind tunnel test section interference related to ground vehicle testing. *SAE paper* 2007-01-1050.
- Wordley, S. and J. Saunders (2008). On-road turbulence. *SAE Paper* 2008-01-0475.